Interplay of Dzyaloshinskii-Moriya and Kitaev interactions for magnonic properties of Heisenberg-Kitaev honeycomb ferromagnets

Li-Chuan Zhang,[1,2,*] Fengfeng Zhu,[3,4] Dongwook Go,[1,5] Fabian R. Lux,[5] Flaviano José dos Santos,[1,6] Samir Lounis,[1,7] Yixi Su,[3] Stefan Blügel,[1] and Yuriy Mokrousov[1,5,†]

[1]*Peter Grünberg Institut and Institute for Advanced Simulation, Forschungszentrum Jülich and JARA, D-52425 Jülich, Germany*

[2]*Department of Physics, RWTH Aachen University, D-52056 Aachen, Germany*

[3]*Jülich Centre for Neutron Science (JCNS) at Heinz Maier-Leibnitz Zentrum (MLZ), Forschungszentrum Jülich, Lichtenbergstrasse 1, D-85747 Garching, Germany*

[4]*Department of Physics and Astronomy, Shanghai Jiao Tong University, Shanghai 200240, China*

[5]*Institute of Physics, Johannes Gutenberg University Mainz, D-55099 Mainz, Germany*

[6]*Theory and Simulation of Materials (THEOS), and National Centre for Computational Design and Discovery of Novel Materials (MARVEL), École Polytechnique Fédérale de Lausanne, CH-1015 Lausanne, Switzerland*

[7]*Faculty of Physics, University of Duisburg-Essen and CENIDE, D-47053 Duisburg, Germany*

(Received 4 January 2021; revised 11 March 2021; accepted 25 March 2021; published 9 April 2021)

The properties of Kitaev materials are attracting ever increasing attention owing to their exotic properties. In realistic two-dimensional materials, the Kitaev interaction is often accompanied by the Dzyaloshinskii-Moriya interaction, which poses a challenge for distinguishing their magnitudes separately. In this paper, we demonstrate that it can be done by accessing magnonic transport properties. By studying honeycomb ferromagnets exhibiting Dzyaloshinskii-Moriya and Kitaev interactions simultaneously, we reveal nontrivial magnonic topological properties accompanied by intricate magnonic transport characteristics as given by thermal Hall and magnon Nernst effects. We also investigate the effect of a magnetic field, showing that it does not only break the symmetry of the system but also brings drastic modifications to magnonic topological transport properties, which serve as hallmarks of the relative strength of anisotropic exchange interactions. Based on our findings, we suggest strategies to estimate the importance of Kitaev interactions in real materials.

DOI: 10.1103/PhysRevB.103.134414

I. INTRODUCTION

Recently, layered magnetic materials with highly anisotropic Kitaev-like spin interactions originated in spin-orbit coupling (SOC) are attracting increasing attention [1–5]. The realization of the celebrated Heisenberg-Kitaev model has been to date verified in layered iridates A_2IrO_3 (A = Li, Na) [6–9], α-RuI_3 [4,10], and CrI_3 [11]. It is known that depending on specific parameters, the Heisenberg-Kitaev model can host gapless or gapped spin-liquid states [4,5], and that a topologically ordered phase can be achieved by applying an external magnetic field [12–14]. This indicates that the Heisenberg-Kitaev model hosts a rich phase diagram [3,15], and as such, Kitaev materials present a promising material platform for the realization of novel applications in the areas of topological quantum computing and spintronics [16,17].

One of the most natural ways to extract the properties of the Kitaev interaction lies in the analysis of the magnon spectra of a given Kitaev material, which naturally incorporates the effect of exchange interactions as well as of the magnetic field [18–20]. However, it has been recently shown that while the Kitaev interaction can realize topological magnon bands in honeycomb ferromagnets [15,21], its effect can be generally similar to that of the SOC-driven Dzyaloshinskii-Moriya interaction (DMI) [22,23]. In fact, the second-nearest-neighbor DMI, which is allowed by symmetry in honeycomb materials [24,25], has been estimated explicitly from *ab initio* calculations of monolayer CrI_3 [26,27]. Therefore, the same magnon dispersion can be interpreted based either on DMI, Kitaev interaction, or their combination. The phase diagram of the Kitaev-DMI model has been studied in the past, and the distinction between the gapped and gapless phases of this model has been shown to be possible to draw by referring to thermal Hall effect measurements [28]. In order to distinguish whether the system is DMI or Kitaev interaction dominated, magnonic properties other than the dispersion have to be investigated in detail.

In this paper, we investigate the magnonic properties of honeycomb ferromagnets exhibiting Kitaev and DMI interactions in the presence of a Heisenberg exchange and magnetocrystalline anisotropy exposed to a magnetic field (see Fig. 1). Based on the topological analysis of the magnonic states, we characterize the spectra of the model and make predictions concerning the behavior of the thermal Hall and magnon Nernst conductivity in response to changes in the parameters of the model, proposing a strategy to distinguish whether the system is dominated by a Kitaev interaction or DMI.

*Corresponding author: li.zhang@fz-juelich.de
†Corresponding author: y.mokrousov@fz-juelich.de

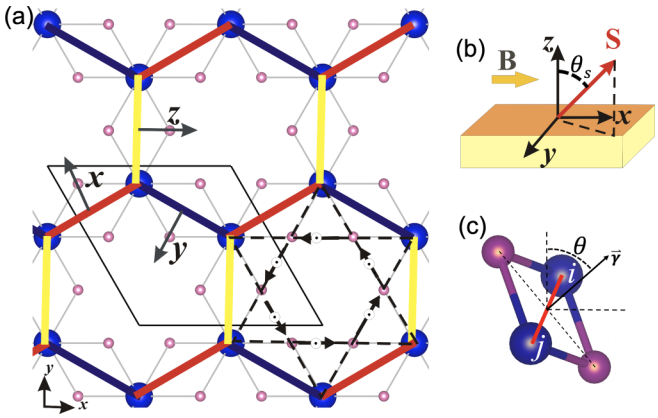

FIG. 1. (a) Sketch of the structure of a honeycomb CrI_3 monolayer. The unit cell is outlined with a thin black line, where blue balls represent Cr^{3+} ions and pink balls are iodide ions. The Kitaev bonds x (red), y (dark blue), z (yellow) are indicated with thick colored lines. The arrows mark the second-nearest-neighbor bond orientations along the black dotted lines that share a common sign of the out-of-plane DM vector. (b) Schematic diagram of the influence of an in-plane magnetic field $\mathbf{B}$ on the spin direction $\mathbf{S}$ whose polar angle is defined as θ_s. (c) The perspective view of the Cr_2I_2 plane, where its normal vector is marked as $\hat{\gamma}$ and the Kitaev angle is defined as the polar angle of $\hat{\gamma}$.

II. MODEL AND METHOD

We consider the effective spin Hamiltonian on a two-dimensional ferromagnetic honeycomb lattice, sketched in Fig. 1, given by

$$H = -\sum_{i,j} J_{ij}\mathbf{S}_i \cdot \mathbf{S}_j - K\sum_{\langle ij\rangle^\gamma} S_i^\gamma S_j^\gamma - \sum_{ij} \mathbf{D}_{ij} \cdot (\mathbf{S}_i \times \mathbf{S}_j) - \sum_i A(\hat{n}_i \cdot \mathbf{S}_i)^2 - \mathbf{B} \cdot \mu_B g \sum_i \mathbf{S}_i, \quad (1)$$

where the J_{ij} coefficients mediate the isotropic Heisenberg exchange interaction between spins $\mathbf{S}_i$ and $\mathbf{S}_j$ on sites i and j, and the second term is due to the anisotropic Kitaev interaction, where $S_i^\gamma = \mathbf{S}_i \cdot \hat{\gamma}_{ij}$ with $\hat{\gamma}_{ij}$ being the Kitaev vector determined by the sites i and j. The second-nearest-neighbor DMI is represented by the third term with DMI vectors $\mathbf{D}_{ij}$ pointing out of plane, as required by the symmetry of the structure, i.e., $\mathbf{D}_{ij} = (0, 0, D_{ij}^z)$. Additionally, we add a single-ion anisotropy term with respect to the local easy axis $\hat{n}_i$ (choosing it to be the unit vector along the z direction), and the energy of Zeeman coupling to the magnetic field $\mathbf{B}$, with μ_B as the Bohr magneton and g-factor of 2.

The structure that we consider here (Fig. 1) is a representative of the Kitaev materials such as α-$RuCl_3$ [4,10] and CrI_3 [11], and for simplicity we refer to our studied system as CrI_3 in the following. Referring to experimental data on the latter material [11], we set approximate values for the nearest-neighbor exchange interaction $J = 0.2$ meV, the Kitaev interaction $K = 5.2$ meV, and the spin moment magnitude $S = 1.5$. We consider an easy-axis anisotropy energy of $A = 0.1$ meV chosen so as to ensure that the ground state is ferromagnetic along the z axis. As displayed in Fig. 1(c), $\hat{\gamma}_{ij}$ is defined as the normal vector to the Cr_2I_2 plane spanned by Cr ions i and j, and the nearby I atoms. Respectively, the Kitaev vector corresponding to the yellow bond in Fig. 1(a) and marked with z is chosen as $\hat{\gamma}_z = (\sin\theta, 0, \cos\theta) = (\frac{\sqrt{2}}{\sqrt{3}}, 0, \frac{1}{\sqrt{3}})$ [11,29], where the Kitaev angle θ is about 54.74° for the case of CrI_3. The Kitaev vectors for red and blue bonds are determined analogously. More details concerning the model can be found in the Supplemental Material (SM) Note 1 [30].

Further, the Holstein-Primakoff transformation [31] is employed to rewrite the Hamiltonian in terms of bosonic ladder operators a_i and $a_i^\dagger$. In the transformed spin-wave Hamiltonian, we keep only the quadratic terms in the spin operators and a Fourier transform of the bosonic ladder operators is performed to rewrite the problem in the momentum space. The Fourier-transformed Hamiltonian, denoted as H_2, thus becomes a $2n \times 2n$ matrix, where $n = 2$ stands for two atoms in the unit cell of honeycomb lattice [32–34]. We diagonalize the dynamical matrix of H_2 based on the commutation relation $i\frac{d\Phi(\mathbf{k})}{dt} = [\Phi(\mathbf{k}), H_2(\mathbf{k})] = D\Phi(\mathbf{k})$, where the dynamical matrix is given by $D = \hat{g}H_2$ with $\hat{g} = [(\mathbb{1}, 0), (0, -\mathbb{1})]$, $\mathbb{1}$ as the $n \times n$ identity matrix, and a basis is chosen as $\Phi(\mathbf{k}) = [a_{1k},\ a_{2k},\ a_{1-k}^\dagger,\ a_{2-k}^\dagger]^T$. Only positive real eigenvalues of the dynamical matrix D are considered and the stability of the system is confirmed when there are two non-negative eigenvalues for each vector $\mathbf{k}$. We employ the magnon Berry curvature formalism to investigate the topological properties of the model, with the magnon Berry curvature of the nth spin-wave branch $\Omega_{n\mathbf{k}}^{xy}$ evaluated according to

$$\Omega_{n\mathbf{k}}^{xy} = -2\,\mathrm{Im}\sum_{m\neq n} \frac{\langle\Psi_{n\mathbf{k}}|\frac{\partial D(\mathbf{k})}{\partial k_x}|\Psi_{m\mathbf{k}}\rangle\langle\Psi_{m\mathbf{k}}|\frac{\partial D(\mathbf{k})}{\partial k_y}|\Psi_{n\mathbf{k}}\rangle}{(\epsilon_{n\mathbf{k}} - \epsilon_{m\mathbf{k}})^2}, \quad (2)$$

where $|\Psi_{n\mathbf{k}}\rangle$ is the right eigenstate of the spin-wave Hamiltonian with the energy $\epsilon_{n\mathbf{k}}$. The topological thermal Hall effect of magnons is the generation of a transverse thermal Hall voltage under an applied longitudinal temperature gradient [35,36]. Based on the expression for the Berry curvature, the transverse thermal Hall conductivity $\kappa_{\mathrm{TH}}^{xy}$ [37] and magnon Nernst conductivity κ_{N}^{xy} [38,39] of the system is calculated (more details are shown in SM Note 3) [30].

III. THE HEISENBERG-KITAEV MODEL

We first ignore the effect of the magnetic field and DMI, and focus on the magnonic transport properties of the simplified Heisenberg-Kitaev model. As the Kitaev angle θ can be different in different Kitaev materials [11,40], we investigate the Heisenberg-Kitaev model by varying the θ angle and the magnitude of K, assuming that the sign of the latter remains positive. We further keep the value of $J + K/3$ constant so as to ensure that the ground state has the same energy. By comparing the band dispersions for different K and θ values shown in Fig. 2(a), we find that the band gap between the two modes $\triangle_K$ is enlarged as either K or θ increases [see Figs. 2(g) and 2(h)]. Meanwhile, a larger K not only decreases the spin stiffness at the Γ point but also opens a larger band gap at $\mathbf{K}$, as shown in Figs. 2(a) and 2(h). As a larger θ enhances the effect of the anisotropic exchange interaction, the single-ion anisotropy energy is introduced to ensure the stability of the system.

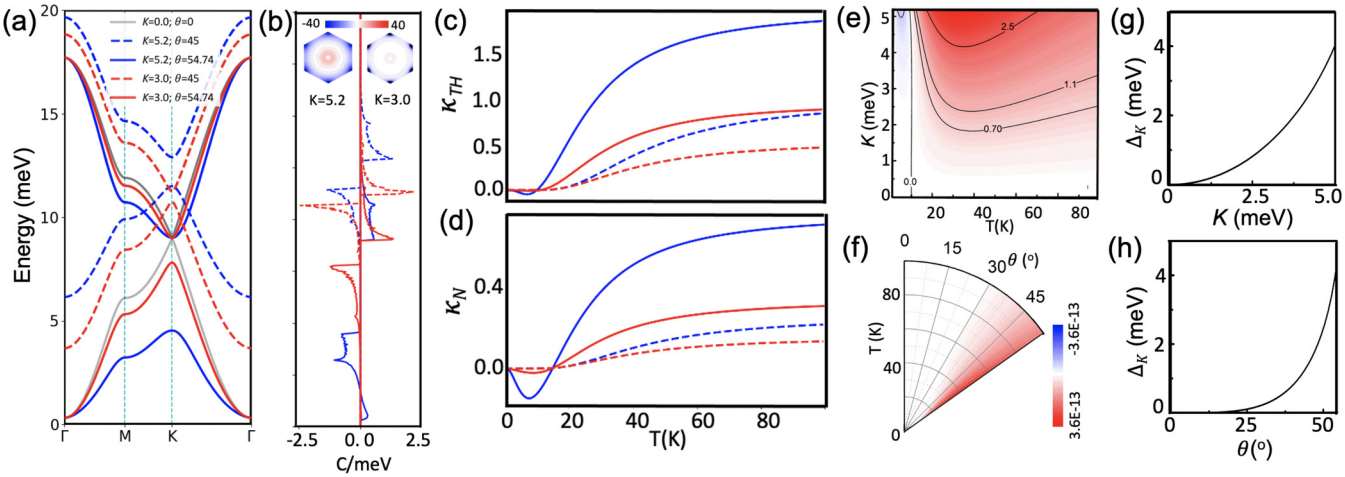

FIG. 2. (a) The comparison of magnon dispersions along high-symmetry lines for different values of the Kitaev parameters. Gray, blue, and red lines correspond to the K values of 0, 5.2, and 3 meV. The dashed and solid lines correspond to the Kitaev angles θ of 45° and 54.74°, respectively. The corresponding energy-resolved Chern number is shown in (b). The Berry curvature distribution of the first magnon branch in the first Brillouin zone for different K values with $\theta = 54.74°$ is shown in the inset of (b). The color map ranges from −40 to 40 in arbitrary (arb.) units, and the exceeding values are marked with black. The temperature dependence of thermal Hall conductivity $\kappa_{\mathrm{TH}}^{xy}$ and magnon Nernst conductivity κ_{N}^{xy} are shown in (c) and (d), in units of 10^{-11} W/K and $k_B/2\pi$, respectively. (e) The map of $\kappa_{\mathrm{TH}}^{xy}/T$ as a function of temperature T and parameter K at the Kitaev angle of $\theta = 54.74°$. (f) The map of $\kappa_{\mathrm{TH}}^{xy}/T$ as a function of T and θ at a constant K value of 5.2 meV. The units of the color maps in (e) and (f) are chosen as $\mathrm{W/K^2}$. The magnon band gap $\triangle_K$ as a function of K (at $\theta = 54.74°$) and θ (at $K = 5.2$ meV) is shown in (g) and (h), respectively.

We address the topological character of the magnonic bands by computing the Chern number C_n, given by $C_n = \frac{1}{2\pi}\int \Omega_{n\mathbf{k}}^{xy}\, d\mathbf{k}$, where the integral is performed over the first Brillouin zone (BZ), and n is the nth magnon branch. The magnonic topology is revealed by computing the Chern numbers to be -1 and $+1$ for the first and second branches in the Heisenberg-Kitaev model, in accord with an existing *ab initio* analysis [41]. As shown in Fig. 2(b), the energy-dependent Chern number defined as an integral of the Berry curvature at a given energy, as well as the Berry curvature distribution of the first branch, indicate that the largest contributions to the Chern number come from around the **K** point. Besides, the observed Chern number variation and Berry curvature distribution are quite nontrivial in energy and in the reciprocal space, which brings about the unusual topological transport properties as manifested in the unusual temperature dependence of the thermal Hall conductivity and the magnon Nernst conductivity.

The thermal Hall conductivity $\kappa_{\mathrm{TH}}^{xy}$ and magnon Nernst conductivity κ_{N}^{xy} are calculated based on the well-known Berry curvature expressions, as discussed in SM Note 3 [30]. The temperature range considered for the analysis of the conductivities is motivated by the fact that the Curie temperature of the system exposed to an external field depends sensitively on the magnitude of J and A, and can reach very sizable values [11]. As shown in Figs. 2(c) and 2(d), a sign change with increasing temperature T of $\kappa_{\mathrm{TH}}^{xy}$ and κ_{N}^{xy} is clearly obtained for the values of $K = 5.2$ meV and $\theta = 54.74°$, which is in line with the observations for Kitaev materials [42,43]. This can be explained by a variation in the sign of the energy-dependent Chern number in the energy region of 1–2 meV for these specific values of K and θ, which is absent for smaller values of Kitaev parameters. For smaller K and θ, the Berry curvature magnitude rises at much higher energies, which explains the overall suppression of thermal Hall and magnon Nernst conductivity that we observe. To emphasize this effect further, we plot the dependence of $\kappa_{\mathrm{TH}}^{xy}/T$ on temperature and parameters K and θ separately in Figs. 2(e) and 2(f). In this figure, we observe that regardless of the sign of $\kappa_{\mathrm{TH}}^{xy}/T$, its absolute value always increases with K and θ at a given temperature. Similar conclusions can be drawn for the magnon Nerst conductivity. In Fig. 2(f), the range of considered angles is limited by 54.75° owing to the fact that the system becomes unstable if the single-ion anisotropy energy remains unchanged. More details concerning the θ dependence of the magnon Nernst effect are provided in SM Note 7 [30].

IV. IMPACT OF DMI

Next, we investigate the impact of DMI on the magnonic transport properties of the Heisenberg-Kitaev model. As shown in Fig. 3(a), our results indicate that both DMI and Kitaev interaction can modify the magnon dispersion and open a gap at the crossing point at **K**. The difference in the impact of DMI and Kitaev interactions is that the latter strongly influences the shape of magnon dispersion, whereas the DMI mainly influences the dispersion around the **K** point. As also visible in Figs. 3(a) and 3(b), a band gap of the same magnitude $\triangle_K$ can be realized by a combination of different DMI and Kitaev parameters. For instance, as shown in Fig. S1 [30], the experimental magnon dispersion of CrI_3 can be fitted well with both the Heisenberg-Kitaev model or Heisenberg-DMI model [11,25]. In this context, the relevance of a given model can be probed by accessing its topological transport properties and comparing them to experiments.

The topological thermal Hall conductivity $\kappa_{\mathrm{TH}}^{xy}$ modulated by Kitaev parameters (θ, K) and DMI (D) is shown in

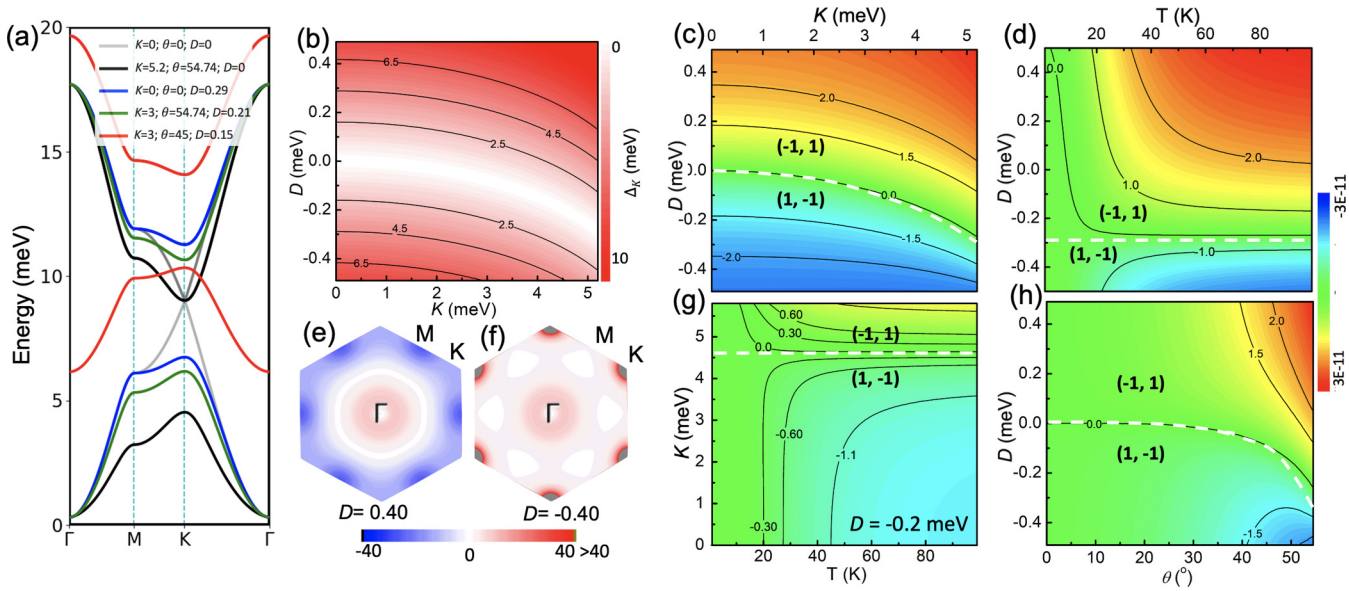

FIG. 3. (a) The comparison of magnon dispersions with different Kitaev and DMI parameters specified in the legend (in the units of meV and degrees). The magnon dispersions represented with black, blue, green, and red lines have almost the same band gap $\triangle_K$ between the two branches. (b) Band gap $\triangle_K$ as a function of D and K at $\theta = 54.74°$. (c) Dependence of thermal Hall conductivity $\kappa_{\mathrm{TH}}^{xy}$ on K and D at $T = 100$ K and $\theta = 54.74°$. The T dependence of thermal Hall conductivity $\kappa_{\mathrm{TH}}^{xy}$ is shown in (d)–(g). (d) $\kappa_{\mathrm{TH}}^{xy}$ as a function of T and D, with K and θ corresponding to the case of CrI_3. (e), (f) The corresponding BZ distribution of the Berry curvature (in arb. units) for the first band with $D = +0.4$ meV (e) and -0.4 meV (f) and the Kitaev interaction is the same as (d). (g) $\kappa_{\mathrm{TH}}^{xy}$ as a function of T and K for $\theta = 54.74°$ and $D = -0.2$ meV. (h) $\kappa_{\mathrm{TH}}^{xy}$ as a function of θ and D at $T = 100$ K and $K = 5.2$ meV. The corresponding color map is in units of W/K.

Figs. 3(c) and 3(d) and Figs. 3(g) and 3(h). The topological phase boundary marking different sets of (C_1, C_2) Chern numbers is shown with a white dashed line. As the sign of the Berry curvature generally changes in the BZ for the first branch [Figs. 3(e) and 3(f)], the zero isoline of $\kappa_{\mathrm{TH}}^{xy}$ does not generally coincide with the phase boundary, which is different from the purely DMI-mediated system [34,37]. Similar to Fig. 2(e), the sign change of $\kappa_{\mathrm{TH}}^{xy}$ is observed with increasing T in Figs. 3(d) and 3(g) in the topological phase marked as $(-1, +1)$. This feature can be explained by the fact that while DMI mainly influences the magnonic states around the **K** or **M** points, the Berry curvature around the **Γ** point is mainly determined by the Kitaev interaction [see Figs. 3(e) and 3(f) and insets of Fig. 2(b)]. The total contribution to $\kappa_{\mathrm{TH}}^{xy}$ thus presents a subtle competition between Berry curvature contributions from around these points, whose overall sign depends on the interplay between the parameters. The phase diagrams of $\kappa_{\mathrm{TH}}^{xy}$ with respect to θ, K, and D at $T = 100$ K are shown in Figs. 3(c) and 3(h). Consistent with the discussion above, the magnitude of $\kappa_{\mathrm{TH}}^{xy}$ is directly determined by the strength of K and magnitude of θ. Notably, at a given K, the sign of $\kappa_{\mathrm{TH}}^{xy}$ can be adjusted by the sense of DMI. Similar observations can be made also for the magnon Nernst conductivity, as shown in Fig. S6 [30].

V. EFFECT OF A MAGNETIC FIELD

Finally, we explore the effect of an external in-plane magnetic field, as shown in Fig. 1(b). As a result of the magnetic field $\mathbf{B} = \mathrm{B}(\cos\phi_s, \sin\phi_s, 0)$ the spins of the Kitaev magnet are inclined into the plane: $\mathbf{S}_i = \mathrm{S}(\sin\theta_s\cos\phi_s, \sin\theta_s\sin\phi_s, \cos\theta_s)$, where θ_s and ϕ_s represent the polar angle and azimuthal angle, respectively. The relationship between the strength of the field B and the inclination angle θ_s is given by $\sin\theta_s = g\mu_B \mathrm{B}/2AS$ (see more details in SM Note 6 [30]).

As shown in Figs. 4(a) and 4(b) and Figs. S7 and S8 [30], both polar angles θ_s and azimuthal angles ϕ_s have an influence on the magnon dispersion. Especially ϕ_s has a strong

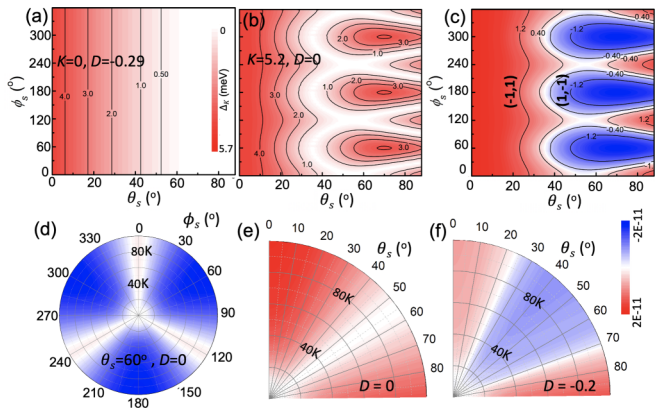

FIG. 4. (a), (b) Evolution of the band gap $\triangle_K$ with the angles θ_s and ϕ_s in the Heisenberg-DMI model ($K = 0$) (a), and Heisenberg-Kitaev model ($D = 0$) (b). (a) and (b) share the same color map and the units are meV. (c) Thermal Hall conductivity $\kappa_{\mathrm{TH}}^{xy}$ as a function of θ_s and ϕ_s at $T = 100$ K [same parameters as in (b)]. (d) $\kappa_{\mathrm{TH}}^{xy}$ as a function of temperature and ϕ_s at $\theta_s = 60°$ and (e), (f) $\kappa_{\mathrm{TH}}^{xy}$ as a function of temperature and θ_s for different values of D assuming $\phi_s = 0°$ and $K = 5.2$ meV. (c)–(f) share the same color map in units of W/T.

impact on the band gap when θ is larger than 40° at finite K, while the band gap is only influenced by the polar angle θ_s in the Heisenberg-DMI model ($K = 0$). Furthermore, the C_3 symmetry of the magnon dispersion is broken if the polar angle is nonzero assuming a nonvanishing Kitaev interaction.

We draw the topological phase diagram of thermal Hall conductivity as a function of θ_s and ϕ_s in Fig. 4(c). When θ_s is smaller than 40°, the system resides in the $(-1, +1)$ phase, and the influence of ϕ_s is suppressed. However, $\kappa_{\mathrm{TH}}^{xy}$ exhibits a very nontrivial dependence on ϕ_s when the system enters the $(+1, -1)$ phase upon increasing θ_s. The strong dependence of $\kappa_{\mathrm{TH}}^{xy}$ on ϕ_s and θ_s is also visible in the temperature-dependence plots shown in Figs. 4(d)–4(f). As becomes apparent from Fig. 4(d), the C_3 symmetry of the conductivity is preserved, in line with the symmetry of the Kitaev interaction on a honeycomb lattice. Moreover, from Figs. 4(e) and 4(f) we observe a strong influence of the DMI on the magnitude and angular dependence of the thermal Hall conductivity. Overall, our results reveal a rich landscape of the thermal Hall effect of Kitaev ferromagnets exposed to an external magnetic field.

VI. DISCUSSION

In our study we investigate the magnonic properties of honeycomb feromagnets with DMI and Kitaev interaction subject to an external magnetic field. On the one hand, we observe intricate magnonic transport characteristics, which have been observed in Kitaev materials [42,43] that we attribute to the nontrivial Berry phase properties of the system. On the other hand, our results demonstrate a rich magnonic topological phase diagram drawn as a function of Kitaev parameters, DMI, and magnetic field strength. Since the magnitude of the latter effects can be adjusted through e.g., application of strain [44] or electric field [45], our investigation provides a good reference point for designing the magnonic properties of candidate Kitaev materials. Our findings bear significant relevance given that although several Kitaev materials have been discovered to date (e.g., Refs. [4,6–10]), it is still not clear how to judge the relative importance of the Kitaev interaction with respect to DMI.

From the perspective of magnons, based on the results of our work, we propose a strategy to disentangle the two types of interactions from each other: If an application of an external in-plane magnetic field brings along a significant modification of the shape of the magnon dispersion and a strong variation of the magnonic properties as a function of the in-plane direction of the field, then the system is dominated by the Kitaev interaction rather than DMI. Additionally, the changes of sign in the thermal transverse characteristics as a function temperature or strength of an external magnetic field can serve as another indication of the prominence of the Kitaev interaction in the system. These simple criteria can potentially enable a magnonic characterization of exchange interactions of Kitaev materials, and pave the way to employing magnonic topology for designing their exotic properties.

ACKNOWLEDGMENTS

This project was supported by the China Scholarship Council (CSC) (Grant No. [2016]3100). The work was also supported by the Deutsche Forschungsgemeinschaft (DFG, German Research Foundation)–Grants No.TRR 173–268565370 (project A11) and No. TRR 288–422213477 (project B06). We acknowledge funding under SPP 2137 "Skyrmionics" of the Deutsche Forschungsgemeinschaft (DFG) and priority Programme SPP 2244 2D Materials - Physics of van der Waals Heterostructures of the DFG (project LO 1659/7-1). We gratefully acknowledge financial support from the European Research Council (ERC) under the European Union's Horizon 2020 research and innovation program (Grant No. 856538, project "3D MAGiC"). We gratefully acknowledge computing time on the supercomputers of Jülich Supercomputing Center, and at the JARA-HPC cluster of RWTH Aachen.

[1] J. Chaloupka, G. Jackeli, and G. Khaliullin, Phys. Rev. Lett. **105**, 027204 (2010).
[2] J. Chaloupka, G. Jackeli, and G. Khaliullin, Phys. Rev. Lett. **110**, 097204 (2013).
[3] L. Janssen, E. C. Andrade, and M. Vojta, Phys. Rev. Lett. **117**, 277202 (2016).
[4] A. Banerjee, C. Bridges, J.-Q. Yan, A. Aczel, L. Li, M. Stone, G. Granroth, M. Lumsden, Y. Yiu, J. Knolle *et al.*, Nat. Mater. **15**, 733 (2016).
[5] Y. Kasahara, T. Ohnishi, Y. Mizukami, O. Tanaka, S. Ma, K. Sugii, N. Kurita, H. Tanaka, J. Nasu, Y. Motome *et al.*, Nature (London) **559**, 227 (2018).
[6] Y. Singh, S. Manni, J. Reuther, T. Berlijn, R. Thomale, W. Ku, S. Trebst, and P. Gegenwart, Phys. Rev. Lett. **108**, 127203 (2012).
[7] S. K. Choi, R. Coldea, A. N. Kolmogorov, T. Lancaster, I. I. Mazin, S. J. Blundell, P. G. Radaelli, Y. Singh, P. Gegenwart, K. R. Choi, S.-W. Cheong, P. J. Baker, C. Stock, and J. Taylor, Phys. Rev. Lett. **108**, 127204 (2012).
[8] F. Ye, S. Chi, H. Cao, B. C. Chakoumakos, J. A. Fernandez-Baca, R. Custelcean, T. F. Qi, O. B. Korneta, and G. Cao, Phys. Rev. B **85**, 180403(R) (2012).
[9] S. H. Chun, J.-W. Kim, J. Kim, H. Zheng, C. C. Stoumpos, C. Malliakas, J. Mitchell, K. Mehlawat, Y. Singh, Y. Choi *et al.*, Nat. Phys. **11**, 462 (2015).
[10] J. Sears, M. Songvilay, K. Plumb, J. Clancy, Y. Qiu, Y. Zhao, D. Parshall, and Y.-J. Kim, Phys. Rev. B **91**, 144420 (2015).
[11] I. Lee, F. G. Utermohlen, D. Weber, K. Hwang, C. Zhang, J. van Tol, J. E. Goldberger, N. Trivedi, and P. C. Hammel, Phys. Rev. Lett. **124**, 017201 (2020).
[12] A. Kitaev, Ann. Phys. **321**, 2 (2006).
[13] H.-C. Jiang, Z.-C. Gu, X.-L. Qi, and S. Trebst, Phys. Rev. B **83**, 245104 (2011).
[14] F. G. Utermohlen and N. Trivedi, arXiv:2012.11604.
[15] P. A. McClarty, X.-Y. Dong, M. Gohlke, J. G. Rau, F. Pollmann, R. Moessner, and K. Penc, Phys. Rev. B **98**, 060404(R) (2018).
[16] C. Nayak, S. H. Simon, A. Stern, M. Freedman, and S. D. Sarma, Rev. Mod. Phys. **80**, 1083 (2008).

[17] I. Žutić, J. Fabian, and S. D. Sarma, Rev. Mod. Phys. **76**, 323 (2004).
[18] L. Wu, A. Little, E. E. Aldape, D. Rees, E. Thewalt, P. Lampen-Kelley, A. Banerjee, C. A. Bridges, J.-Q. Yan, D. Boone *et al.*, Phys. Rev. B **98**, 094425 (2018).
[19] N. Janša, A. Zorko, M. Gomilšek, M. Pregelj, K. W. Krämer, D. Biner, A. Biffin, C. Rüegg, and M. Klanjšek, Nat. Phys. **14**, 786 (2018).
[20] J. Cenker, B. Huang, N. Suri, P. Thijssen, A. Miller, T. Song, T. Taniguchi, K. Watanabe, M. A. McGuire, D. Xiao *et al.*, Nat. Phys. **17**, 20 (2021).
[21] D. G. Joshi, Phys. Rev. B **98**, 060405(R) (2018).
[22] I. Dzyaloshinsky, J. Phys. Chem. Solids **4**, 241 (1958).
[23] T. Moriya, Phys. Rev. **120**, 91 (1960).
[24] S. K. Kim, H. Ochoa, R. Zarzuela, and Y. Tserkovnyak, Phys. Rev. Lett. **117**, 227201 (2016).
[25] L. Chen, J.-H. Chung, B. Gao, T. Chen, M. B. Stone, A. I. Kolesnikov, Q. Huang, and P. Dai, Phys. Rev. X **8**, 041028 (2018).
[26] C. Xu, J. Feng, S. Prokhorenko, Y. Nahas, H. Xiang, and L. Bellaiche, Phys. Rev. B **101**, 060404(R) (2020).
[27] S. I. Vishkayi, Z. Torbatian, A. Qaiumzadeh, and R. Asgari, Phys. Rev. Materials **4**, 094004 (2020).
[28] Y. H. Gao, C. Hickey, T. Xiang, S. Trebst, and G. Chen, Phys. Rev. Research **1**, 013014 (2019).
[29] E. Aguilera, R. Jaeschke-Ubiergo, N. Vidal-Silva, L. Foa, and A. Núñez, Phys. Rev. B **102**, 024409 (2020).
[30] See Supplemental Material at http://link.aps.org/supplemental/10.1103/PhysRevB.103.134414 for technical details of the calculations.
[31] T. Holstein and H. Primakoff, Phys. Rev. **58**, 1098 (1940).
[32] S. Toth and B. Lake, J. Phys.: Condens. Matter **27**, 166002 (2015).
[33] F. J. dos Santos, M. dos Santos Dias, F. S. M. Guimarães, J. Bouaziz, and S. Lounis, Phys. Rev. B **97**, 024431 (2018).
[34] L.-C. Zhang, Y. A. Onykiienko, P. M. Buhl, Y. V. Tymoshenko, P. Čermák, A. Schneidewind, J. R. Stewart, A. Henschel, M. Schmidt, S. Blügel, D. S. Inosov, and Y. Mokrousov, Phys. Rev. Research **2**, 013063 (2020).
[35] Y. Onose, T. Ideue, H. Katsura, Y. Shiomi, N. Nagaosa, and Y. Tokura, Science **329**, 297 (2010).
[36] M. Hirschberger, R. Chisnell, Y. S. Lee, and N. P. Ong, Phys. Rev. Lett. **115**, 106603 (2015).
[37] A. Mook, J. Henk, and I. Mertig, Phys. Rev. B **89**, 134409 (2014).
[38] A. A. Kovalev and V. Zyuzin, Phys. Rev. B **93**, 161106(R) (2016).
[39] V. A. Zyuzin and A. A. Kovalev, Phys. Rev. Lett. **117**, 217203 (2016).
[40] C. Xu, J. Feng, H. Xiang, and L. Bellaiche, npj Comput. Mater. **4**, 1 (2018).
[41] A. T. Costa, D. L. R. Santos, N. M. Peres, and J. Fernández-Rossier, 2D Mater. **7**, 045031 (2020).
[42] Y. Kasahara, K. Sugii, T. Ohnishi, M. Shimozawa, M. Yamashita, N. Kurita, H. Tanaka, J. Nasu, Y. Motome, T. Shibauchi *et al.*, Phys. Rev. Lett. **120**, 217205 (2018).
[43] R. Hentrich, M. Roslova, A. Isaeva, T. Doert, W. Brenig, B. Büchner, and C. Hess, Phys. Rev. B **99**, 085136 (2019).
[44] C. Xu, J. Feng, M. Kawamura, Y. Yamaji, Y. Nahas, S. Prokhorenko, Y. Qi, H. Xiang, and L. Bellaiche, Phys. Rev. Lett. **124**, 087205 (2020).
[45] T. Koyama, Y. Nakatani, J. Ieda, and D. Chiba, Sci. Adv. **4**, eaav0265 (2018).